

The Structure of Mouse Cytomegalovirus m04 Protein Obtained from Sparse NMR Data Reveals a Conserved Fold of the m02-m06 Viral Immune Modulator Family

Nikolaos G. Sgourakis,¹ Kannan Natarajan,² Jinfa Ying,¹ Beat Vogeli,^{1,3} Lisa F. Boyd,² David H. Margulies,^{2,*} and Ad Bax^{1,*}

¹Laboratory of Chemical Physics, National Institute of Diabetes and Digestive and Kidney Diseases, National Institutes of Health, Bethesda, MD 20892, USA

²Molecular Biology Section, Laboratory of Immunology, National Institute of Allergy and Infectious Diseases, National Institutes of Health, Bethesda, MD 20892, USA

³Present address: Laboratory of Physical Chemistry, Swiss Federal Institute of Technology, 8093 Zurich, Switzerland

*Correspondence: dhm@nih.gov (D.H.M.), bax@nih.gov (A.B.)

<http://dx.doi.org/10.1016/j.str.2014.05.018>

SUMMARY

Immuno-evasins are key proteins used by viruses to subvert host immune responses. Determining their high-resolution structures is key to understanding virus-host interactions toward the design of vaccines and other antiviral therapies. Mouse cytomegalovirus encodes a unique set of immuno-evasins, the m02-m06 family, that modulates major histocompatibility complex class I (MHC-I) antigen presentation to CD8⁺ T cells and natural killer cells. Notwithstanding the large number of genetic and functional studies, the structural biology of immuno-evasins remains incompletely understood, largely because of crystallization bottlenecks. Here we implement a technology using sparse nuclear magnetic resonance data and integrative Rosetta modeling to determine the structure of the m04/gp34 immuno-evasin extracellular domain. The structure reveals a β fold that is representative of the m02-m06 family of viral proteins, several of which are known to bind MHC-I molecules and interfere with antigen presentation, suggesting its role as a diversified immune regulation module.

INTRODUCTION

Cytomegaloviruses (CMVs) are important models of pathogen-host interactions, widely recognized for their ability to interfere with host immune responses to accomplish the multifaceted task of inhibiting the recognition of infected cells by CD8⁺ T cells while avoiding destruction by natural killer (NK) cells according to the “missing-self” hypothesis (i.e., the lack of antigen-presenting major histocompatibility complex class I [MHC-I] molecules on the cell surface) (Lemmermann et al., 2012). To do this, the virus maintains a series of genes encoding immune evasion and regulatory proteins (Lilley and Ploegh, 2005). In particular, the m02-m16 family is a class of early-expressed genes of mouse CMV (MCMV) crucial for viral survival and infec-

tivity. However, there is no identifiable homology to any determined structure in the Protein Data Bank (PDB), nor is there amino acid sequence similarity to any other protein family. A member of the m02-m06 class, the m04/gp34 protein, is unique in its ability to bind MHC-I molecules in the endoplasmic reticulum (ER) and accompany them to the cell surface (Kleijnen et al., 1997), while the closely related m06 protein binds MHC-I and directs it to the endosome (Tomas et al., 2010). Therefore, it has been proposed that by countering the MHC-retaining functions of other viral proteins (m06 and the MHC-I-like m152), m04 helps MCMV evade the NK cell response (Babić et al., 2010, 2011; Holtappels et al., 2006). The combined effects of m04, m06, and m152 on CD8⁺ T cells and NK responses reveal a complex and still poorly understood aspect of MCMV immune evasion (Pinto et al., 2006). Although the structural basis for the function of m152/gp40 immuno-evasin has been previously revealed by X-ray crystallography (Wang et al., 2012), and structures of other MCMV MHC-I-like proteins have been similarly characterized (Adams et al., 2007; Berry et al., 2013; Mans et al., 2007; Natarajan et al., 2006), for other molecules, a detailed picture is still lacking because of difficulties in crystallization and the large sizes of their in vivo functional complexes, making conventional nuclear magnetic resonance (NMR) studies challenging. In particular, extensive crystallization trials in our laboratory using different constructs of m04 have repeatedly failed to yield well-diffracting protein crystals.

Recent advances in computational methods using the program Rosetta (Leaver-Fay et al., 2011) allow accurate modeling of protein structures from sparse NMR data sets containing chemical shifts (CSs), residual dipolar couplings (RDCs), and a minimal subset of the proton-proton distances used by conventional methods (Shen et al., 2008). By combining the use of CS-Rosetta with extensive deuteration of side-chain protons to improve ¹³C relaxation and the use of transverse relaxation optimized spectroscopy (TROSY) at high magnetic fields to improve ¹⁵N and amide ¹H relaxation (Pervushin et al., 1997), the structure of larger proteins and protein complexes can now be determined by solution NMR (Raman et al., 2010; Sgourakis et al., 2011). Methyl protons are reintroduced using site-specific labeling of Ile, Leu, and Val (ILV) residues (Tugarinov et al., 2006), a scheme that greatly simplifies the NMR spectra while still providing a sparse set of long-range methyl-methyl nuclear

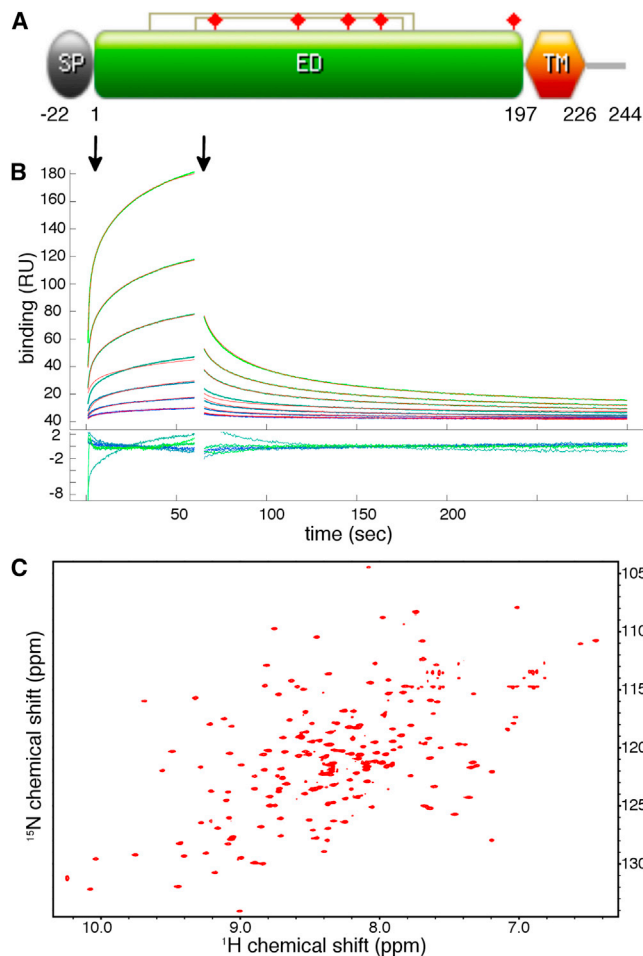


Figure 1. Biophysical Characterization of m04ED for Structural Studies

(A) Domain organization of full-length m04/gp34, indicating the positions of SP, ED, and TM domain. Disulfide bonds are indicated with connected lines and glycosylation sites with filled red prisms.

(B) SPR binding sensograms collected using immobilized m04ED (WT) with increasing concentrations of H2-D^d flowthrough, as outlined in [Experimental Procedures](#). The start of the injection (association) and washout (dissociation) phases are indicated with vertical arrows. The data were fit using EVILFIT (Svitel et al., 2003) (thin red lines; $K_d \sim 395 \mu\text{M}$). Residual errors in the fit are shown in the inset. As a negative control, the MHC-I-like molecule MULT-1 was injected over the same SPR surface ([Figure S1](#)).

(C) TROSY-HSQC ¹H-¹⁵N correlation spectra of m04ED -C7S recorded at 900 MHz, 12°C, and pH 6.5.

Overhauser effects (NOEs) as structural restraints. In addition, the use of the resolution-adapted structural recombination (RASREC) algorithm within Rosetta greatly enhances the sampling of nonlocal features such as long-range contacts through β pairings (Bradley and Baker, 2006) and allows structural convergence in systems with complicated backbone topologies and high contact order (Lange and Baker, 2012). RASREC-Rosetta offers clear advantages over conventional simulated annealing protocols in terms of both performance and convergence: In a benchmark set of five proteins of sizes 15 to 40 kDa with known crystal structures, RASREC guided by ILV

data was found to outperform conventional protocols in terms of both precision (convergence) and accuracy relative to the target structure (Lange et al., 2012). This is due in part to the use of an empirically optimized all-atom energy function that defines the local hydrogen-bonding and side-chain-packing features once a sufficiently converged low-resolution model of the backbone (within 2–5 Å accuracy relative to the native structure) can be obtained using a sparse network of long-range experimental restraints. Thus, although experimental data are still required to define an overall backbone fold, Rosetta alleviates the need for extensive side-chain assignments and a high density of NOE restraints (in excess of ten restraints per residue) that is typically required by conventional protocols. For larger, more challenging systems in which the sparse ILV and amide-amide NOE data are insufficient to determine conclusively the target backbone structure, obtaining RDCs from spectra gathered in multiple alignment media is a powerful way to improve further structural convergence and validate the final Rosetta models, as shown in recent RASREC applications (Rao et al., 2014; Warner et al., 2011). Recent TROSY-based methods allow quantitative RDC measurements for larger proteins at high accuracy (Fitzkee and Bax, 2010).

Here we combine these advanced NMR technologies to determine the structure of the m04 extracellular domain (m04ED). The calculations converge to a well-defined structure showing an elaborate β sheet topology that is reminiscent of, but highly divergent from, the canonical immunoglobulin (Ig) fold (Williams and Barclay, 1988). Sequence alignments with other members of the viral m02-m06 family show that the structural features of the m04 core are broadly conserved among members of this family, suggesting that the interactions involved in MHC-I binding are likely to be similar as well.

RESULTS

The m04ED Binds MHC-I Molecules

m04 was originally identified as a 34 kDa glycoprotein that coimmunoprecipitates with MHC-I molecules upon MCMV infection (Kleijnen et al., 1997). Toward determining the molecular requirements of m04 recognition by MHC, previous studies have highlighted the requirement for proper MHC folding and association with its light-chain β_2 -microglobulin to accommodate m04 binding, suggesting that m04 interacts with properly conformed, peptide-loaded MHC-I molecules (Lu et al., 2006). This work further suggested that the transmembrane (TM) region of m04 is critical for its interaction with the MHC-I molecule H2-K^b. To test whether this is a general feature of m04-MHC interactions and to identify a minimal, functional m04 construct suitable for structural studies by NMR, we expressed the ED of the m04 protein (m04ED), excluding the signal peptide (SP), the TM region, and the intracellular C-terminal tail ([Figure 1A](#)). The protein was expressed in *E. coli* and therefore also lacked the posttranslational glycosylations present in the wild-type (WT) protein (WT m04 has five consensus glycosylation sites, of which three have been confirmed to be used in vivo [Kleijnen et al., 1997]). To evaluate the biological activity of recombinant m04 protein, we examined its interaction with the MHC-I molecule H2-D^d by surface plasmon resonance (SPR). Preliminary SPR experiments ([Figure 1B](#)) demonstrate a direct but weak ($K_D \geq 100 \mu\text{M}$)

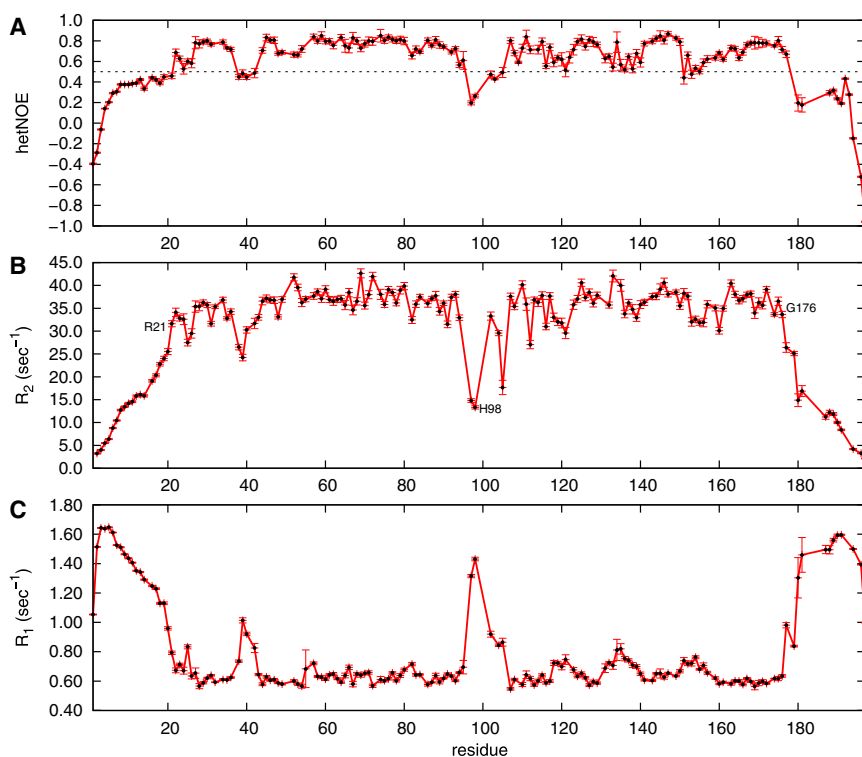


Figure 2. ^{15}N Amide Relaxation Rates and $^{15}\text{N}\text{-}\{^1\text{H}\}$ NOE Ratios for the Full-Length m04ED Sequence, Recorded at 600 MHz ^1H Frequency

(A–C) R_2 values were obtained from measured $R_{1\rho}$ rates after correction for off-resonance effects (Massi et al., 2004). Key residues that demarcate the structural core (21–176) and flexible loop region (95–102) are highlighted on the plots. The dotted line in (A) indicates the 0.5 $^{15}\text{N}\text{-}\{^1\text{H}\}$ NOE cutoff value used to define rigid and dynamic structural elements within the m04ED molecule.

interaction between m04ED and the MHC-I molecule H2-D^d, even in the absence of the TM region and posttranslational modifications. By contrast, the MHC-I-like molecule, MULT-1, used here as a negative control, did not bind (Figure S1 available online).

Our results reveal a measurable interaction between MHC and the m04 ectodomain using a direct biophysical method. Previous studies demonstrated the requirement of the m04 TM region for efficient m04-MHC interaction in detergent cell lysates (Lu et al., 2006). Taken together, these results support a model of weak interaction between the luminal domains when strongly coupled via their TM domains.

NMR Backbone Relaxation Rates Identify a Well-Ordered Structural Core

The optimized m04ED construct shows well-dispersed 2D $^1\text{H}\text{-}^{15}\text{N}$ heteronuclear single-quantum coherence (HSQC) spectra indicative of a folded, stable protein core (Figure 1C). We used backbone relaxation experiments to probe the extent of backbone conformational dynamics on the fast (picoseconds to nanoseconds) timescale (Kay et al., 1989). The resulting ^{15}N R_1 and R_2 (Figures 2B and 2C) relaxation rates combined with the heteronuclear $^{15}\text{N}\text{-}\{^1\text{H}\}$ NOE (Figure 2A) indicate the presence of a well-ordered structural core spanning residues 21 to 176, which includes a flexible loop at residues 95 to 102. The N-terminal region (residues 1–20) is highly mobile on the nanosecond timescale, as evidenced by decreased $^{15}\text{N}\text{-}\{^1\text{H}\}$ NOE and increased R_1 and decreased R_2 relaxation rates. This highly charged segment (11 of 20 charged residues) includes 3.5 turns of a regular α helix for residues 6 to 19, as indicated by the analysis of backbone CSs using the program TALOS-N (Shen and

Bax, 2013), and the presence of short-range $d_{\alpha\text{N}}(i,i+3)$ and $d_{\text{NN}}(i,i+1)$ NOE patterns (Wuthrich, 1986), confirming the α -helical structure. The elevated dynamic characteristics and the absence of long-range $\text{H}^{\text{N}}\text{-}\text{H}^{\text{N}}$ or $\text{H}^{\text{N}}\text{-}\text{CH}_3$ NOEs to core residues suggest that the N-terminal helix interacts only transiently with the core. Similarly, the C-terminal residues 177 to 197 are highly mobile on the picosecond-to-nanosecond timescale, as indicated by the ^{15}N relaxation data. This region is found primarily in a disordered loop/coil conformation that, like the N terminus, does not participate in strong packing interactions with the core structure. Taken together, these results reveal the presence of a well-ordered protein fold for residues 21 to 176, flanked by two terminal-capping sequences. We therefore focus on determining the structure of this m04ED core region to elucidate its fold and identify structural features that could serve as possible binding sites for MHC-I molecules.

Rosetta Structure Determination Using RDCs and Sparse ILV NOE Data

Toward obtaining a converged structure of the m04ED core, we performed a number of iterative CS-Rosetta calculations by progressively increasing the number of experimental restraints supplied (Table 1; Figure 3). First, using only the backbone CSs and 23 long-range $\text{H}^{\text{N}}\text{-}\text{H}^{\text{N}}$ NOEs (Table 1, No. 1; Figure 3A) we obtained a preliminary structure of the m04ED core, in which the first 130 residues (residues 21–150) converged to a well-defined fold. This fold consists of a five-stranded antiparallel β sheet platform (with the β -pairing topology $\beta_1\text{-}\beta_9\text{-}\beta_4\text{-}\beta_5\text{-}\beta_6$), a shorter antiparallel four-stranded sheet ($\beta_2\text{-}\beta_3\text{-}\beta_8\text{-}\beta_7$) packing underneath the upper side of the platform, and connecting loops of different lengths, with a six-residue helical segment located in the $\beta_8\text{-}\beta_9$ loop that connects the bottom and top β sheets (as outlined in Figure 6D). Two disulfide bonds at residues 26 to 147 ($\beta_1\text{-}\beta_9$) and 47 to 142 ($\beta_3\text{-}\beta_9$) stabilize the tertiary fold. Analysis of the $^{13}\text{C}^\alpha$ and $^{13}\text{C}^\beta$ CSs of the four Cys residues confirms their oxidized state. Although the CSs help define the local backbone conformation, the long-range $\text{H}^{\text{N}}\text{-}\text{H}^{\text{N}}$ NOEs constrain the β -pairing topology. Several salient features of the structure, including a β bulge centered at Asp72 of strand β_4 and a bend at Leu88 of strand β_5 , are supported by the NOE

Table 1. Summary of Iterative CS-Rosetta Structure Calculations

No.	Experimental Restraints Used	Converged Residues ^a	$F_{\text{converged}}$ (%)	$\langle E_{\text{Rosetta}} \rangle^b$	$\langle Q_{\text{work}} \rangle$	$\langle Q_{\text{free}} \rangle^c$	Ct-Helix ^d
1	NOE _{amide}	24–94, 102–117, 123–149	73	-212 ± 4	1.43	1.23	top ^e
2	NOE _{amide} , RDC ₁	23–94, 105–170	89	-224 ± 2	0.40	0.68	under
3	NOE _{amide} , RDC ₁ , RDC ₂	21–95, 103–170	91	-231 ± 4	0.37/0.41	NA	under
4	NOE _{amide} , NOE _{met-amide} , RDC ₁	21–94, 103–174	94	-225 ± 3	0.38	0.58	under
5	NOE _{amide} , NOE _{met-amide} , NOE _{met-met}	21–94, 102–117, 123–172	90	-230 ± 3	0.54	0.80	under
6	NOE _{amide} , NOE _{met-amide} , NOE _{met-met} , RDC ₁	21–94, 103–174	94	-229 ± 1	0.44	0.60	under
7	NOE _{amide} , NOE _{met-amide} , NOE _{met-met} , RDC ₁ , RDC ₂	21–94, 103–175	95	-236 ± 4	0.36/0.40	NA	under

^aBelow 3 Å backbone rmsd in the ten lowest energy models.

^bAverage and SD computed over the ten lowest energy models, in Rosetta energy units.

^cComputed using an independent RDC data set not used in the structure calculations. NA indicates that all available RDC data were used as restraints.

^dPlacement of the C-terminal α -helical segment (residues 160–171) relative to the extended β sheet platform.

^eThis segment is not converged within 3 Å backbone rmsd.

and CS data and confirm the power of the Rosetta structure determination protocol for this highly sparse NOE data set (1.5 long-range restraints per 10 residues). The remaining 26 C-terminal residues of the core sequence (151–176) were poorly converged in the first round of models, as no long-range H^N-H^N NOEs could be identified for this part of the sequence. Analysis of the backbone CSs using TALOS-N (Shen and Bax, 2013) indicates that this segment contains three turns of an α helix (residues 160–171).

To better define the conformation of the C-terminal helix, we measured RDCs in two alignment media (Pf1 phage and positively charged gel) that report on the orientation of N-H vectors with respect to an overall alignment frame (Bax and Grishaev, 2005). The two data sets are complementary in the sense that the two alignment tensors show a normalized scalar product (Sass et al., 2000) of only 0.51 (corresponding to a 60° angle in five-dimensional alignment tensor space), meaning that the two measurements are quite independent of each other. Additionally, the linear correlation between the raw RDC data sets is 0.36, further suggesting that the two data sets are for all practical purposes sufficiently independent (Figure S2C) (Tolman and Ruan, 2006). Inspection of the RDCs for core residues 160 to 171 (Figure S2A and S2B) reveals a kink in the C-terminal helix, centered at Ser167, in which the helical axis changes orientation by an angle of $\sim 60^\circ$. This trend is consistent between the two RDC data sets and is further supported by the backbone CS data. We then performed two sets of calculations (Table 1, Nos. 2 and 3) using the RDCs in addition to the H^N-H^N NOEs and backbone CSs. In the first run, we used only RDCs from the Pf1-aligned sample, while reserving the second RDC data set, measured in positively charged gel, for validation. The calculations resulted in a better converged C terminus (backbone rmsd within 3 Å), in which the kinked α helix packs underneath strands β_1 and β_9 of the lower end of the extended β sheet platform, with hydrophobic contacts mediated by the side chains of Met162, Leu163, Met166, Val169, Leu170, and Leu172 (Figure 3B). This placement of the C-terminal kinked helix cross-validates well with respect to the second, unused RDC data set (Q_{free} [Cornilescu et al., 1998] of 0.68 versus 1.23 for the first-round models [constructed with no RDC restraints], corresponding to a Pearson's linear correlation coefficient R_P of 0.72 [Cornilescu and Bax, 2000]). However, even with the

inclusion of the second RDC data set as weak restraints in the calculation, the convergence of the C-terminal helix was insufficient to define an atomic model (i.e., with a backbone rmsd of < 2 Å), because of the lack of long-range NOEs for the helical residues 160–171 (Table 1, No. 3).

We then recorded additional 3D NOE spectra using a sparsely labeled ILV sample with the aim of improving structural convergence for the C-terminal segment and to allow further validation of the structure. Careful analysis of the spectra revealed a total of 19 long-range H^N-CH₃ NOEs that were included in the subsequent round of calculations (Table 1, No. 4). This set includes five restraints from Asp159, Val168, Leu169, and Leu172 that link the C-terminal helix to the main core of the structure (Figures 4B and 4D), while the remaining 14 restraints validate the β sheet topology obtained in the previous models. The resulting models show improved convergence of the C terminus (backbone rmsd within 1.5 Å), and RDC cross-validation statistics ($Q_{\text{free}} = 0.58$, $R_P = 0.82$). Finally, we identified 25 long-range CH₃-CH₃ NOEs in the corresponding methyl NOE spectra, 6 of which map to the C-terminal α helix (Figures 4A and 4C), validating the previous round of models (Table 1, Nos. 5–7). All NOE cross-peaks with peak signal-to-noise ratios > 10 , which also showed mirror peaks in the case of HN(N)H, (H)NNH, H(C)CH, and (H)CCH 3D NOE spectra, were manually assigned and classified as intraregion, sequential or medium range (which further validated the backbone and methyl resonance assignments), or long range, corresponding to a sequence separation greater than five residues. Although the short- to medium-range NOEs were consistent with the first-round Rosetta models, the inclusion of such restraints in the calculations does not lead to any gains in convergence of the local backbone structure, which is already heavily constrained by the CS data. Including all the available long-range NOEs, backbone CSs and RDC data (Table 1, No. 7) led to a structural ensemble (Figure 3C) that is converged to within a backbone rmsd of 0.85 Å, excluding the loop region spanning residues 95 to 102 (Figure S3B). This loop is highly mobile on the picosecond-to-nanosecond timescale, as evidenced by the reduced ¹⁵N-¹H NOE values (Figure S3A) and further supported by the near-zero RDC values (Figures S2A and S2B). We find that the use of RDC restraints strongly improves convergence for the backbone core spanning residues 21 to 176 (95%, with the remaining 5% of the sequence

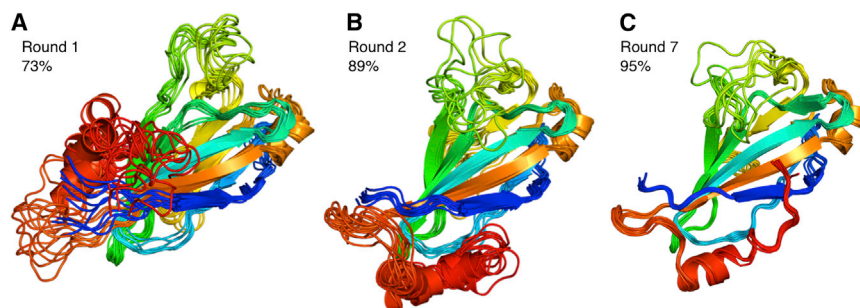


Figure 3. Convergence of the m04ED Core Structure at Different Phases of the Structure Determination Process

(A–C) Ribbon diagrams of the 10 lowest energy models at selected stages of CS-Rosetta/RASREC structure calculations outlined in Table 1. Each ensemble is superimposed on the coordinates of the lowest energy model and colored blue to red from N to C terminus. The fraction of residues converged within 3 Å backbone rmsd is indicated in each diagram. The final ensemble of (C) is converged to an average backbone rmsd of 0.85 Å, excluding the flexible loop region spanning residues 95–102.

corresponding to the flexible loop at residues 95–102), including a short, ordered loop at residues 118 to 122 (Table 1, compare No. 5 with Nos. 6 and 7). The open, type-I' conformation of the loop (Figure 5B) is supported by analysis of the backbone CSs (Shen and Bax, 2012) and further validated by the absence of a long range H^N-H^N NOE between Leu49 and Asn122 that would be expected for an alternative closed conformation sampled in the RDC-free calculations (Figure 5A). The final full-atom models (Tables 1, No. 7, and 2; Figure 3C) have good packing and structural statistics (assessed separately using MOLPROBITY [Chen et al., 2010]) while satisfying all experimental NOE restraints and showing good fits to both RDC data sets (Figures S4A and S4B).

The m04 Core Structure Exemplifies a Highly Diverse Ig-Based Immunoepitope Fold

m04 does not show any homology to nonviral proteins by amino acid sequence comparisons or to any sequence of known structure in the PDB. At first sight, the m04 core resembles the fold of the Ig superfamily, which can be further divided into four to nine main structural classes (Bateman et al., 1996; Halaby et al., 1999) depending on overall size, strand connectivity, and loop size. A Dali (Holm and Rosenström, 2010) search using the NMR structure as a target suggests a statistically significant structural similarity (Z score ≤ 5.0) to a variety of Ig-like molecules (Igs) such as various antibody chains (e.g., PDB accession number 1AXS-chain B) and human leukocyte antigen class-II Ig-like domains (e.g., PDB accession number 4H1L-chain H). Moreover, the disulfide bond at C142–C47 with Trp62 packing against it and the β strand arrangement are clearly indicative of an Ig fold. However, a closer look at the structural alignments reveals major differences from the canonical Ig superfamily.

Although the Ig fold is typically characterized by seven strands on two sheets (Structural Classification of Proteins [Andrejeva et al., 2008]), the m04 core structure has a total of nine strands, four of which (β_2 – β_3 – β_8 – β_7) are short (4 or 5 residues each) and form one layer of the β sandwich, while five strands of 6 to 12 residues in length (β_1 – β_9 – β_4 – β_5 – β_6) form an extended β sheet platform on the other side of the sandwich (Figure 6D). The five-stranded platform provides a nucleus beneath which the smaller four-stranded sheet packs at its upper end. The kinked C-terminal helix supports the lower end of the larger five-stranded platform. In addition, the strand connectivity is clearly different from the closest Ig fold, found in the antibody variable (V) domains (typically an A[β_1], B[β_2], E[β_5], D[β_4] sheet packed

against C[β_3], F[β_6], G[β_7]). Furthermore the spacing between the Cys residues forming the disulfide bond that links the two β layers (typically between the B and F strands) (Cys47, Cys142) is significantly larger than found in Igs (95 versus 55–75 residues) and connects β_3 to β_9 . Finally, m04 has one additional disulfide bond connecting Cys26 (β_1) and Cys147 (β_9). These features, specifically the secondary structural elements forming the hydrophobic core of the fold and the second disulfide, are highly conserved in the m02–m06 family and among different MCMV strains (Corbett et al., 2007) (Figure 7). In particular, this family preserves the NAXWXXE/HW motif (in strand β_4) throughout a large number of laboratory and wild-derived isolates of MCMV. This segment is a central element of the m04 fold, likely to play a key role in stabilizing the core structure, which provides a scaffold for the grafting of various loop sequences among different family members. Taken together, these results suggest that the m04 structure is likely a product of convergent evolution toward an Ig-like structure rather than a true structural homolog of Igs.

DISCUSSION

This description of the solution structure of the m04/gp34 glycoprotein ED reveals the power of a hybrid methodology that combines multidimensional NMR with sparse labeling and data collection techniques and integrative computational modeling (Ward et al., 2013). The value of progressive addition of experimental data sets in achieving a converged set of minimum energy structures is documented here and highlights the importance of including ILV NOEs and RDCs in the proper placement of structural elements. In particular, these distance and orientational restraints permitted the placement of the C-terminal α -helical segment to a defined position underlying a β sheet platform and precise modeling of a second loop conformation. The dynamic aspects of the m04ED structure revealed by NMR relaxation experiments, notably the highly mobile amino and carboxy-terminal segments as well as the central loop region, may relate to the function of the molecule in its ability to interact with a number of diverse MHC-I molecules as well as the difficulty in identifying suitable crystallization conditions.

The overall structure of m04ED reveals a complex β topology, punctuated with connecting regions containing both coil and helix, distantly related to the Ig fold. This core β structure permits variation in the connecting loops, as evidenced by the amino acid sequence diversity observed in other members of the

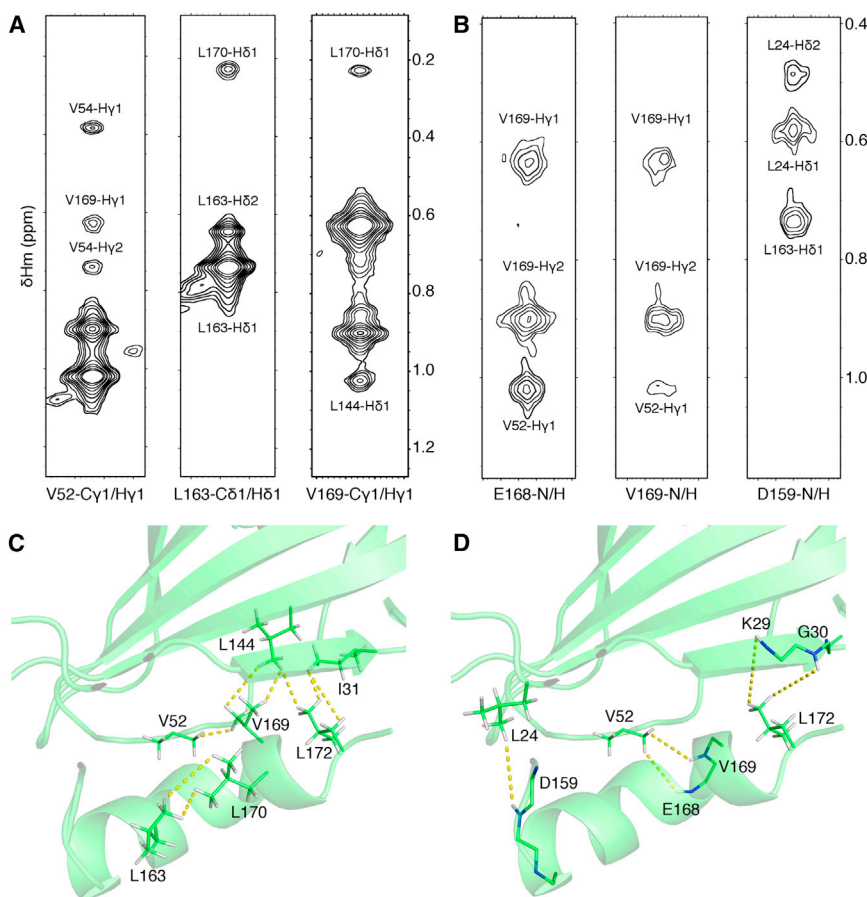


Figure 4. ILV NOE Structural Restraints Used to Determine the Placement of the C-Terminal Helix

(A and B) Representative ¹H-¹H strips from the CH₃-CH₃ (A) or H^N-CH₃ (B) NOESY 3D ¹H-separated spectra, recorded using an ILV-labeled sample.

(C and D) Structure diagrams indicating the position of long-range CH₃-CH₃ (C) and H^N-CH₃ NOEs (D) involving at least one residue from the C-terminal helix, residues 159 to 172.

The same ¹H ppm y-scale is used for all NOE strips within (A) and (B), as indicated in the axis of the last strip from each group. The strips were drawn at the ppm values corresponding to the methyl (A) or amide (B) atom pair assignments indicated below each panel, with each x axis centered on the H^m (A) or H^N (B) assigned CS values. In (A), the first and second most intense peaks correspond to the diagonal (self-peak) and second methyl group within the same spin system, respectively. The assignments of each additional NOE cross-peak are further indicated. The spectra were contoured using ten levels spaced by factors of 1.4, starting at a height equal to 2 times the background noise. The lowest energy model in the final NMR ensemble was used in (C) and (D).

Immunoprecipitation experiments of MCMV-infected cells demonstrate that m04 is the major component associated with MHC-I molecules (Kleijnen et al., 1997). Biochemical experiments indicate the importance of a functional peptide-

m02-m06 viral protein family, and should prove useful in designing crystallizable variants toward determining the structures of other family members. The closely related m06 also carries out an immunomodulatory function and binds MHC-I molecules (Reusch et al., 1999). Amino acid sequence analysis of the extended family that includes m02-m16 has suggested that all of these genes encode structurally related proteins, and the structure of m04ED provides a toehold in deriving their structures. Whether the structural similarities carry over to related functions or the m04 structure serves as a robust scaffold for loop variability offering novel function remains to be determined.

m04/gp34 is posttranslationally processed in the ER and contains at least three N-asparaginyl-linked carbohydrate moieties (Kleijnen et al., 1997). We have determined the NMR structure of m04 using a bacterially expressed construct, so it is important to consider the predicted location of the N-asparaginyl sites in the context of this structure. An analysis of the amino acid sequence of m04 using the NetNGlyc 1.0 Server (Blom et al., 2004) identifies seven potential N-X-S/T sites in m04ED, of which five, at positions 5, 32, 55, 116, and 131, are likely to be used. The core of m04ED contains four of these sites, and the locations of the Asn residues on the amino acid sequence alignment and on the ribbon diagram of the structure are shown in Figures 6 and 7. All of the glycosylation sites are located in accessible loop regions and are not expected to interfere with the proper folding of the core structure.

loading apparatus (including transporter associated with antigen processing and tapasin) as well as the TM region of m04 for the association (Lu et al., 2006). Our experiments, using a truncated m04 construct lacking the TM and cytoplasmic regions of the protein, indicate that the m04ED is sufficient for a transient interaction with MHC-I and that the m04ED may contribute to interaction with the luminal domain of assembled MHC-I heterotrimers (MHC-I heavy chain, β₂ m, and peptide). The apparent low affinity of the m04ED interaction with soluble MHC-I contrasts with the results of immunoprecipitation experiments of virus-infected or transfectant cell lysates, in which m04 is a predominant MHC-I-associated molecule (Kleijnen et al., 1997; Lu et al., 2006). These differences may also result from the clear differences in measurement of association of molecules constrained by 2D membrane surfaces as compared with 3D solution measurements. Alternatively, in addition to the demonstrated role of the TM regions, we cannot rule out the participation of additional cellular or viral components in this interaction. Inspection of the structure and consideration of other molecules that interact with MHC-I and MHC-I-like molecules (T cell receptors, CD8 coreceptor, NK receptors, and other viral immunoevasins including m152, US2, CV203, and E3-19K glycoprotein) prompts us to speculate on possible m04ED sites that might participate in MHC-I interactions. Examination of the surface electrostatic potential of m04ED (Figure 6B) suggests that the large basic groove along the

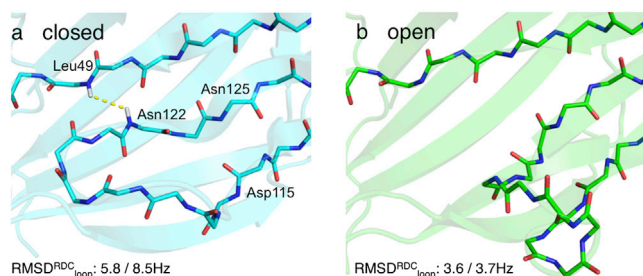


Figure 5. Possible Loop Conformations for Residues D115-1N125
(A and B) Closed (A) and open (B) loop conformations sampled in Rosetta structure calculations using only the sparse NOE distance restraints (A) or NOEs supplemented by amide RDCs from two alignment media (B). The rms of the residual χ^2 in the RDC structure fits (Pf1/gel) is indicated for each conformation. A strong H^N-H^N NOE cross-peak between the well-resolved resonances of Leu49 and Asn122 (indicated with a yellow line in [A]) expected in the “closed” conformation was not observed in the H(N)NH and (H)NNH NOESY spectra, further supporting the “open” loop conformation. Although the NOE data alone are insufficient to define the loop, convergence to the “open” conformation is obtained when RDC restraints are included in addition to NOEs.

platform of the five-stranded β sheet formed by Arg143 and Arg145 on β_9 and Arg89 on β_6 may accommodate an extended acidic region of the MHC-I, like the conserved region observed on many MHC-I α_3 domains, and particularly notable on H2-D^d (Achour et al., 1998; Li et al., 1998; Wang et al., 2002). The MHC footprint on m04 and vice versa can be mapped using high-resolution NMR, as shown previously for interactions involving the T cell receptor (Duchardt et al., 2007; Varani et al., 2007), an approach that is currently pursued in our laboratory using labeled H2-D^d.

The novelty of the m04 fold, the lack of homologous amino acid sequences in any genomic database (including genomes of the closely related rat CMV [Vink et al., 2000]), and the preservation of a range of related family members in a number of different MCMV isolates raise the question as to whether the m02-m06 family has arisen uniquely in the MCMVs and rapidly expanded because of its utility, or that CMVs of other species lost members of the family because of lack of selective advantage. For example, the closely related K181, G4, and Smith MCMV strains all have functional m02-m06 genes, while strains G1F and MI6A have substituted m03.5 for m03, and strains W8211 and W8 have both m03 and m03.5 in addition to m02, m04-m06 (Corbett et al., 2007). The availability of an m02 family paradigm structure not only may contribute to a detailed understanding of the basis of its MHC regulatory function but may provide insight into the expansion and contraction of immunomodulatory viral gene families (Smith et al., 2013).

EXPERIMENTAL PROCEDURES

Sample Preparation for SPR and NMR

DNA encoding m04 was PCR amplified from virus containing cell culture supernatants and has the sequence of the K181 laboratory strain of MCMV (Uniprot ID A2Q6L0), with the additional mutations I31V, I44V. m04ED was expressed in *E. coli* as insoluble inclusion bodies, denatured in 6M guanidine-HCl, refolded in vitro, and purified by size exclusion and ion-exchange

Table 2. NMR Restraints and Structural Statistics

NMR Distance, Orientation, and Dihedral Angle Restraints	
Distance restraints	
Total NOE (long range)	67
H^N-H^N	23
$H^N-CH_3^a$	19
$CH_3-CH_3^a$	25
Total dihedral angle restraints ^b	
Φ	146
Ψ	146
Total RDC restraints	
Data set 1 (Pf1)	119
Data set 2 (gel)	112
Structural Statistics ^{c,d}	
RDC Q-factors	
Data set 1 (Pf1)	0.36
Data set 2 (gel)	0.40
Average rmsd (\AA) ^c	
Backbone	0.85
All heavy atom	1.25

^aNot stereospecifically assigned.

^bUsed to bias the selection of 3-mer and 9-mer backbone fragments, as outlined in Experimental Procedures.

^cComputed over the ten lowest energy structures, excluding the loop region at residues 95 to 105.

^dNo NOE violations (distance > 4.0 \AA between interacting sites) present in the final ensemble.

chromatography. The final sample conditions for NMR were 0.5 mM m04ED, 50 mM NaCl in 20 mM NaH_2PO_4 buffer (pH 6.5). The quality of the 2D $^1\text{H}-^{15}\text{N}$ HSQC correlation spectra was further improved by the single C7S mutation, leading to well-resolved spectra free of conformational exchange line broadening. However, protein degradation and aggregation limited sample life to 3 to 5 weeks, even while keeping the sample at a relatively low temperature of 12°C during NMR data collection. The ED of H2-D^d and mouse β_2 -microglobulin for SPR studies were expressed, refolded with the synthetic decamer peptide p18-110 (RGPGRAFVTI), and purified as described previously (Wang et al., 2009).

SPR Measurements

SPR binding studies were carried out on a Biacore T100 System (GE Healthcare Life Sciences) in which a CM5 Sensor chip was derivatized with 6,300 resonance units (RU) of recombinant m04ED. The purified m04ED protein was coupled to the dextran surface of a CM5 sensor chip at a density of 1,000 RU, following standard N-hydroxysuccinimide/N-ethyl-N'-(3-dimethylaminopropyl) carbodiimide hydrochloride activation and covalent coupling at pH 5.0 (Corr et al., 1993). Graded concentrations of H2-D^d/p18-110 (Figure 1B) or MULT-1, used here as a negative control (Figure S1), prepared and purified as outlined above, were then injected over the m04 surface in HBST buffer (HBS-EP, 10 mM HEPES [pH 7.4], 0.15 M NaCl, 3 mM EDTA, 0.05% surfactant P20). For MULT-1, concentrations were 38.76 μM , 19.4 μM , 9.7 μM , 4.85 μM , 2.4 μM , and 1.2 μM ; for H2-D^d/p18-110/ β_2 m, 21.5 μM , 10.75 μM , 5.4 μM , 2.7 μM , 1.35 μM , 0.67 μM , and 0.335 μM . Analyte proteins were offered to the coupled surfaces at a flow rate of 30 $\mu\text{l}/\text{min}$, for 60 s, at which time washout was initiated and carried out for 600 s. Regeneration of the m04ED surface was carried out with a 30 s pulse of 0.5M NaCl followed by reequilibration for 100 s in running buffer. Data were corrected for background binding to a mock coupled surface and analyzed with EVILFIT (Svitel et al., 2003).

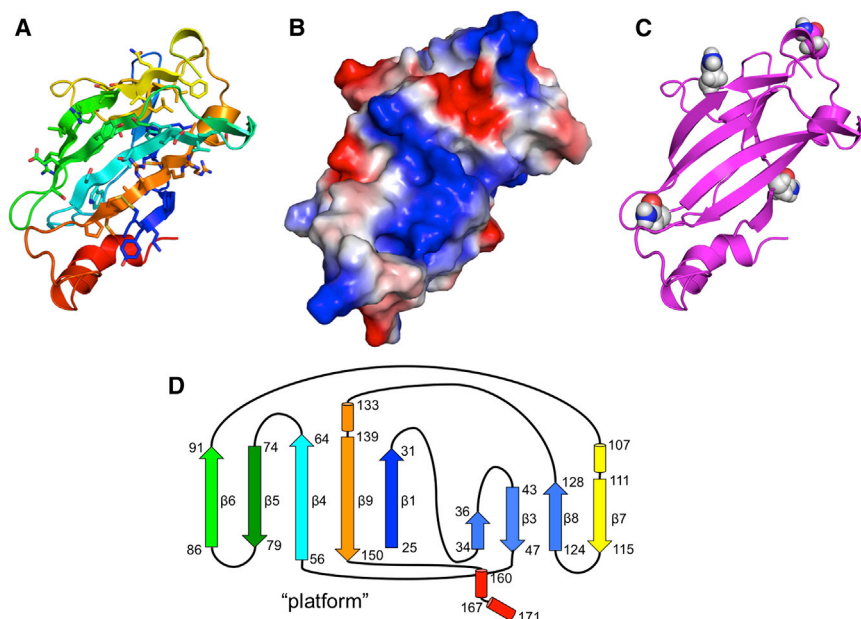


Figure 6. m04ED Core Structure Summary

(A) m04ED core NMR structure indicating the position of side chains on the conserved β sheet platform. The extended loop residues (95–102) have been omitted for improved viewing.

(B) Vacuum electrostatics surface computed using Adaptive Poisson Boltzmann Solver (Baker et al., 2001), shown in the same molecular orientation of the platform as in (A).

(C) High-confidence predicted glycosylation sites using NetNGlyc (Blom et al., 2004).

(D) β sheet connectivity diagram for the m04ED core structure. β strands are drawn as arrows and short α helices as cylinders. The position of the “platform” β sheet from (A) is indicated on the diagram.

and attenuated spectra. All backbone relaxation spectra were recorded at 600 MHz.

RDC Measurements

We measured RDCs under two different alignment conditions. Initially, we explored a 15 mg/ml Pf1

phage sample, but this resulted in strong overalignment of m04 due to electrostatic interactions of the positively charged protein (+8) with the highly negatively charged phage particles. To circumvent this problem, we decreased the Pf1 concentration to 7.5 mg/ml, while increasing the salt concentration to 200 mM. Under these conditions, Pf1 is in the paranematic phase region, where the alignment strength (measured by the residual ^2H quadrupole splitting of the lock solvent) scales with the strength of the magnetic field (Zweckstetter and Bax, 2001), which was further used as a handle to adjust the alignment strength to a desirable range while retaining good spectral resolution. Amide RDCs from transverse relaxation-optimized spectroscopy (ARTSY) (Fitzkee and Bax, 2010) spectra were recorded at 600 MHz, leading to a 28 Hz range of final RDC values. We obtained a complementary RDC data set in positively charged 5.5% w/v acrylamide/bis-acrylamide stretched gel (Chou et al., 2001) (containing 6%w/v DADMAC-14) by recording ARTSY spectra at 800 MHz, leading to a 26 Hz range of RDC values (Figure S2). As a figure of merit for the goodness of fit of the models to the experimental RDC data, we used the Q factor (Clare and Garrett, 1999; Cornilescu et al., 1998), which reports the deviation of the back-calculated RDCs from the raw data, relative to a range of RDCs estimated from a randomly distributed set of vectors assuming an alignment tensor of known D_a and R parameters:

$$Q = \frac{\text{RMS}(D_{\text{calc}} - D_{\text{obs}})}{\sqrt{D_a^2(4 + 3R^2)}/5}$$

where D_a and R refer to the magnitude and rhombicity of the alignment tensor, and D_{calc} and D_{obs} are the calculated and observed dipolar couplings, respectively. Q_{free} is the Q factor computed for a linearly independent RDC data set, not used in the structure calculations. Pearson's linear correlation coefficient R_P is defined as

$$R_P = \frac{\text{cov}(D_{\text{calc}}, D_{\text{obs}})}{\sigma_{D_{\text{calc}}} * \sigma_{D_{\text{obs}}}}$$

where $\text{cov}(D_{\text{calc}}, D_{\text{obs}})$ is the covariance between the individual computed and calculated RDCs, and $\sigma_{D_{\text{calc}}}$, $\sigma_{D_{\text{obs}}}$ are the SDs of the experimental and computed RDCs, respectively.

Iterative CS-Rosetta Structure Calculations

We used the recently developed RASREC protocol (Lange and Baker, 2012), guided by the backbone CSs, a total of 67 long-range NOE distance restraints (23 $\text{H}^{\text{N}}-\text{H}^{\text{N}}$, 25 CH_3-CH_3 , and 19 $\text{H}^{\text{N}}-\text{CH}_3$) and 231 RDCs from two alignment media as N-H vector orientation restraints. In summary, the approach is based on several cycles of Monte Carlo-based trials, which include the sampling of

NMR Backbone, Side-Chain Assignments, Backbone Relaxation Rates, and ILV NOE Measurements

All experiments were recorded at a temperature of 12°C using 600 MHz, 800 MHz, and 900 MHz cryoprobe-equipped Bruker spectrometers. We used an array of standard triple-resonance assignment experiments (HNCO, HN[CA]CO, HNCA, and HNCACB) supplemented with H(N)NH and (H)NNH 3D NOE spectroscopy (NOESY) data sets, recorded at 600 MHz using a mixing time of 250 ms. All resulting spectra were processed with NMRPipe (Delaglio et al., 1995) and analyzed with Sparky (<http://www.cgl.ucsf.edu/home/sparky/>). Orthogonal projections from each 3D data set were extracted on the basis of the centered HNCO peak positions and visualized using the strip-plotting interface in nmrDraw (scroll.tcl), obtaining a highly consistent network of final assignments, with a completeness > 95% (excluding Pro residues). The strip-plot visualization allowed identification of 23 strong long-range $\text{H}^{\text{N}}-\text{H}^{\text{N}}$ NOEs, sufficient to define a protein fold for the m04ED core, as outlined in detail in the structure calculation section.

To assign selectively labeled ILV methyls, we used the SIM-HMCM(CGCBACA)CO (Tugarinov et al., 2014) and HMCM(CG)CBACA (Tugarinov and Kay, 2003) triple-resonance spectra recorded at 600 MHz that link the methyl resonances to the previously established backbone C' and $\text{C}^{\beta}/\text{C}^{\alpha}$ resonance assignments, respectively. These experiments were performed using a deuterated sample that was specifically ^{13}C labeled at the side chains of ILV residues such as to yield a linear spin system (Tugarinov et al., 2006). In this manner, we obtained complete assignments for all 66 labeled $\text{C}^{\delta 1}$, $\text{C}^{\delta 1}/\text{C}^{\delta 2}$, and $\text{C}^{\gamma 1}/\text{C}^{\gamma 2}$ methyls in the m04 sequence (containing 2 Ile, 16 Leu, and 16 Val residues, respectively), which were identified in a high-resolution methyl heteronuclear multiple-quantum coherence spectrum obtained at 900 MHz using a separate ILV sample that was ^{13}C labeled only at the methyl carbon atoms (Figure S5). Finally, using the same sample, we recorded two complementary 3D methyl-to-amide NOESY spectra at 900 MHz and two methyl-to-methyl NOESY data sets at 600 MHz using 250 and 200 ms mixing times, respectively. The processed methyl NOE data further validated the methyl assignments and provided a total of 44 long-range contacts (19 $\text{H}^{\text{N}}-\text{CH}_3$ and 25 CH_3-CH_3) that were manually picked and readily assigned using Sparky.

Backbone amide ^{15}N R_1 relaxation rates and heteronuclear NOE ratios were measured from a perdeuterated, amide ^1H sample using TROSY-readout methods (Lakomek et al., 2012). R_2 rates were obtained from rotating-frame $R_{1\rho}$ rates (Massi et al., 2004) measured under a spin-lock field strength of 2 kHz, after correction for the ^{15}N off-resonance, tilted field. Uncertainties in the R_1 and $R_{1\rho}$ measurements were estimated from the spectral noise levels using 21 Monte Carlo simulations, while uncertainties in the heteronuclear NOE ratios were propagated directly from the noise levels in the reference

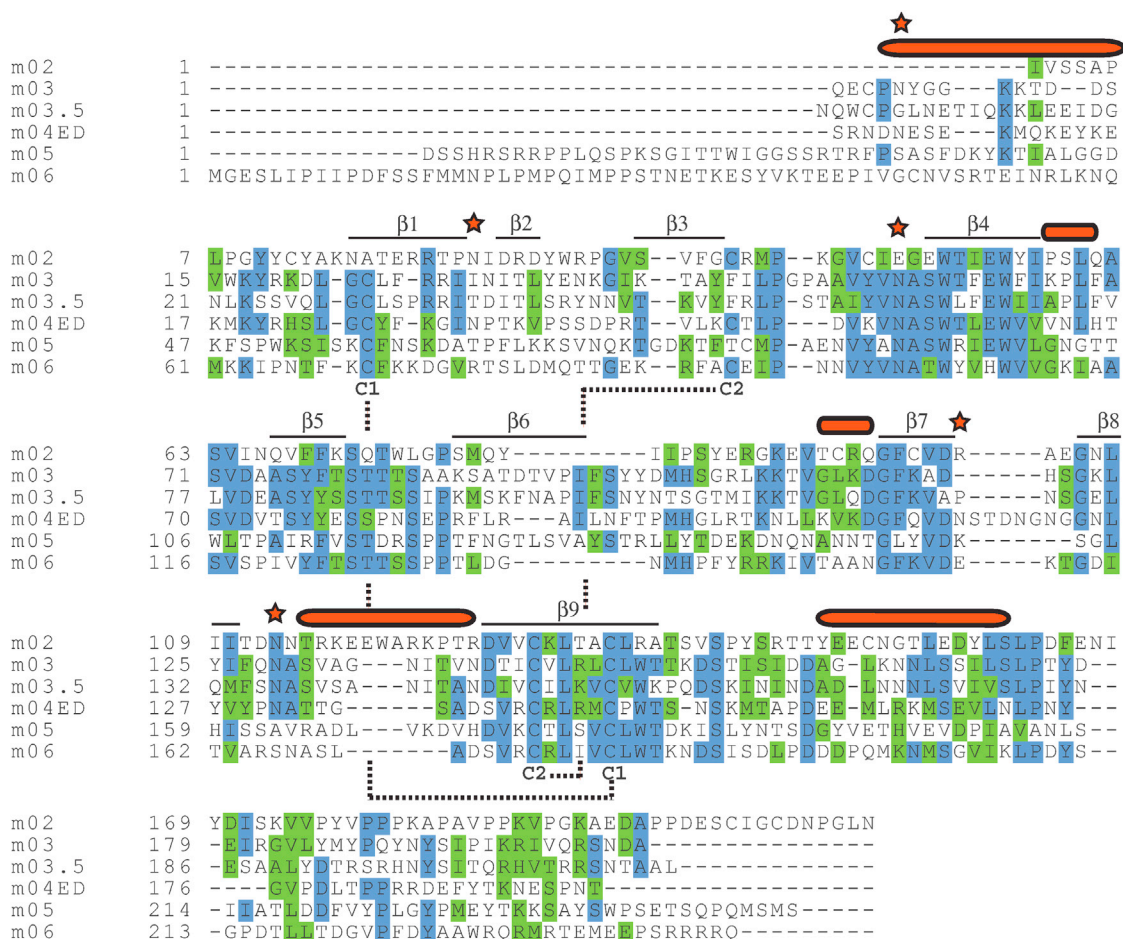


Figure 7. Multiple Sequence Alignment of m04ED with the Predicted EDs of Other m02-m06 Family Members

The approximate positions of conserved secondary structure elements are highlighted on the top of each alignment block (β_1 – β_9 ; β strands; red ovals: α helices). The position of the two disulfide bonds on the m04ED structure is indicated with capital C letters and connecting dashed lines, while high-confidence predicted glycosylation sites on the m04ED sequence are indicated with stars. Protein sequences for m02 (UniProt ID YP_214010), m03 (YP_214011), m05 (YP_214013), and m06 (YP_214014) were all taken from the Smith MCMV genome (NC_004065). The sequence of m03.5 (ABM74010), not present in the Smith strain, was taken from strain G1F.

To identify the ER-luminal domains of these proteins from the full-length protein sequence, we first identified the end of the SP using the SignalP (<http://www.cbs.dtu.dk/services/SignalP/>) and Phobius (<http://phobius.sbc.su.se/>) servers, then identified the start of TM domains using TMPred (http://www.ch.embnet.org/software/TMPRED_form.html). Sequence alignments were constructed using ClustalW2 (<http://www.ebi.ac.uk/Tools/msa/clustalw2/>) and colored by sequence similarity using BoxShade (http://www.ch.embnet.org/software/BOX_form.html).

backbone fragments (3-mers and 9-mers) and β strand pairings. Structural features that consistently lead to optimization of a target function (defined as the sum of the Rosetta energy and the experimental NOE and RDC score terms) are recombined during six generations of iterative structure calculations. In a series of benchmark calculations with targets of known structures, the protocol showed improved sampling efficiency over both standard CS-Rosetta structure calculations (Shen et al., 2008) and conventional NMR structure determination programs (Herrmann et al., 2002) for β -rich proteins with complicated topologies (Lange et al., 2012).

While the backbone CSs are used to guide the selection of backbone fragments from high-resolution structures in the PDB (Vernon et al., 2013), long-range NOEs help define the overall protein fold and β strand connectivity. RDCs are used as bond vector orientation restraints relative to an overall alignment frame to better define the local backbone structure, particularly in loop regions that have few or no long-range NOEs. The calculations are heavily restrained by the experimental data during the low-resolution backbone search. However, the final placement of side-chain rotamers and fine-tuning of the backbone torsion angles is guided primarily by the Rosetta

energy function (Leaver-Fay et al., 2011), with almost no bias from the experimental score terms.

NOEs were implemented as flat-bottom restraints with an upper limit of 4.0 Å and an exponential penalty function. In the absence of stereospecific methyl proton assignments, all pairwise combinations of protons within each pair of interacting methyl sites were averaged as r^{-6} to compute an effective NOE distance (Nilges, 1993). In all calculations, the connectivity of disulfide bonds was also used as an input restraint using an orientation-dependent potential (Raman et al., 2009). All calculations were carried out in 200 threads of an SGI UV2000 cluster using Intel Xeon E5-4640 processors at 2.40 GHz with 1,024 GB of memory, customized to accommodate the MPI interface required by RASREC. Typical calculation runtimes under these conditions were 10 to 12 hr.

ACCESSION NUMBERS

The final 10 lowest energy models were deposited in the PDB (accession number 2MIZ).

SUPPLEMENTAL INFORMATION

Supplemental Information includes five figures and can be found with this article online at <http://dx.doi.org/10.1016/j.str.2014.05.018>.

ACKNOWLEDGMENTS

We thank Dr. Oliver Lange for providing consultation with setting up the RASREC-Rosetta protocol and Dr. Vitali Tugarinov for assistance with the SIM-HMCM(CGBCA)CO and HMCM(CG)CBCA triple-resonance experiments. We are grateful to Drs. Nathan May for preparing multiple sequence alignments of the m02 family and to Drs. Yang Shen and Lishan Yao for preliminary work on determining optimal m04 sample conditions, as well as to Dr. Manqing Hong for providing the MULT-1 protein sample. This work is supported by the National Institute of Diabetes and Digestive and Kidney Diseases and National Institute of Allergy and Infectious Diseases intramural research programs and the Intramural AIDS-Targeted Antiviral Program of the Office of the Director, NIH.

Received: March 6, 2014
 Revised: May 23, 2014
 Accepted: May 27, 2014
 Published: August 7, 2014

REFERENCES

- Achour, A., Persson, K., Harris, R.A., Sundbäck, J., Sentman, C.L., Lindqvist, Y., Schneider, G., and Kärre, K. (1998). The crystal structure of H-2Dd MHC class I complexed with the HIV-1-derived peptide P18-110 at 2.4 Å resolution: implications for T cell and NK cell recognition. *Immunity* 9, 199–208.
- Adams, E.J., Juo, Z.S., Venook, R.T., Boulanger, M.J., Arase, H., Lanier, L.L., and Garcia, K.C. (2007). Structural elucidation of the m157 mouse cytomegalovirus ligand for Ly49 natural killer cell receptors. *Proc. Natl. Acad. Sci. U S A* 104, 10128–10133.
- Andreeva, A., Howorth, D., Chandonia, J.M., Brenner, S.E., Hubbard, T.J., Chothia, C., and Murzin, A.G. (2008). Data growth and its impact on the SCOP database: new developments. *Nucleic Acids Res.* 36, D419–D425.
- Babić, M., Pyzik, M., Zafirova, B., Mitrović, M., Butorac, V., Lanier, L.L., Krmpotić, A., Vidal, S.M., and Jonjić, S. (2010). Cytomegalovirus immunoevasin reveals the physiological role of “missing self” recognition in natural killer cell dependent virus control in vivo. *J. Exp. Med.* 207, 2663–2673.
- Babić, M., Krmpotić, A., and Jonjić, S. (2011). All is fair in virus-host interactions: NK cells and cytomegalovirus. *Trends Mol. Med.* 17, 677–685.
- Baker, N.A., Sept, D., Joseph, S., Holst, M.J., and McCammon, J.A. (2001). Electrostatics of nanosystems: application to microtubules and the ribosome. *Proc. Natl. Acad. Sci. U S A* 98, 10037–10041.
- Bateman, A., Eddy, S.R., and Chothia, C. (1996). Members of the immunoglobulin superfamily in bacteria. *Protein Sci.* 5, 1939–1941.
- Bax, A., and Grishaev, A. (2005). Weak alignment NMR: a hawk-eyed view of biomolecular structure. *Curr. Opin. Struct. Biol.* 15, 563–570.
- Berry, R., Ng, N., Saunders, P.M., Vivian, J.P., Lin, J., Deuss, F.A., Corbett, A.J., Forbes, C.A., Widjaja, J.M., Sullivan, L.C., et al. (2013). Targeting of a natural killer cell receptor family by a viral immunoevasin. *Nat. Immunol.* 14, 699–705.
- Blom, N., Sicheritz-Pontén, T., Gupta, R., Gammeltoft, S., and Brunak, S. (2004). Prediction of post-translational glycosylation and phosphorylation of proteins from the amino acid sequence. *Proteomics* 4, 1633–1649.
- Bradley, P., and Baker, D. (2006). Improved beta-protein structure prediction by multilevel optimization of nonlocal strand pairings and local backbone conformation. *Proteins* 65, 922–929.
- Chen, V.B., Arendall, W.B., 3rd, Headd, J.J., Keedy, D.A., Immormino, R.M., Kapral, G.J., Murray, L.W., Richardson, J.S., and Richardson, D.C. (2010). MolProbity: all-atom structure validation for macromolecular crystallography. *Acta Crystallogr. D Biol. Crystallogr.* 66, 12–21.
- Chou, J.J., Gaemers, S., Howder, B., Louis, J.M., and Bax, A. (2001). A simple apparatus for generating stretched polyacrylamide gels, yielding uniform alignment of proteins and detergent micelles. *J. Biomol. NMR* 21, 377–382.
- Clore, G.M., and Garrett, D.S. (1999). R-factor, free R, and complete cross-validation for dipolar coupling refinement of NMR structures. *J. Am. Chem. Soc.* 121, 9008–9012.
- Corbett, A.J., Forbes, C.A., Moro, D., and Scalzo, A.A. (2007). Extensive sequence variation exists among isolates of murine cytomegalovirus within members of the m02 family of genes. *J. Gen. Virol.* 88, 758–769.
- Cornilescu, G., and Bax, A. (2000). Measurement of proton, nitrogen, and carbonyl chemical shielding anisotropies in a protein dissolved in a dilute liquid crystalline phase. *J. Am. Chem. Soc.* 122, 10143–10154.
- Cornilescu, G., Marquardt, J.L., Ottiger, M., and Bax, A. (1998). Validation of protein structure from anisotropic carbonyl chemical shifts in a dilute liquid crystalline phase. *J. Am. Chem. Soc.* 120, 6836–6837.
- Corr, M., Boyd, L.F., Padlan, E.A., and Margulies, D.H. (1993). H-2Dd exploits a four residue peptide binding motif. *J. Exp. Med.* 178, 1877–1892.
- Delaglio, F., Grzesiek, S., Vuister, G.W., Zhu, G., Pfeifer, J., and Bax, A. (1995). NMRPipe: a multidimensional spectral processing system based on UNIX pipes. *J. Biomol. NMR* 6, 277–293.
- Duchardt, E., Sigalov, A.B., Aivazian, D., Stern, L.J., and Schwalbe, H. (2007). Structure induction of the T-cell receptor zeta-chain upon lipid binding investigated by NMR spectroscopy. *ChemBioChem* 8, 820–827.
- Fitzkee, N.C., and Bax, A. (2010). Facile measurement of ¹H-¹⁵N residual dipolar couplings in larger perdeuterated proteins. *J. Biomol. NMR* 48, 65–70.
- Halaby, D.M., Poupon, A., and Mornon, J. (1999). The immunoglobulin fold family: sequence analysis and 3D structure comparisons. *Protein Eng.* 12, 563–571.
- Herrmann, T., Güntert, P., and Wüthrich, K. (2002). Protein NMR structure determination with automated NOE assignment using the new software CANDID and the torsion angle dynamics algorithm DYANA. *J. Mol. Biol.* 319, 209–227.
- Holm, L., and Rosenström, P. (2010). DALI server: conservation mapping in 3D. *Nucleic Acids Res.* 38, W545–W549.
- Holtappels, R., Gillert-Marien, D., Thomas, D., Podlech, J., Deegen, P., Herter, S., Oehrlein-Karpi, S.A., Strand, D., Wagner, M., and Reddehase, M.J. (2006). Cytomegalovirus encodes a positive regulator of antigen presentation. *J. Virol.* 80, 7613–7624.
- Kay, L.E., Torchia, D.A., and Bax, A. (1989). Backbone dynamics of proteins as studied by 15N inverse detected heteronuclear NMR spectroscopy: application to staphylococcal nuclease. *Biochemistry* 28, 8972–8979.
- Kleijnen, M.F., Huppa, J.B., Lucin, P., Mukherjee, S., Farrell, H., Campbell, A.E., Koszinowski, U.H., Hill, A.B., and Ploegh, H.L. (1997). A mouse cytomegalovirus glycoprotein, gp34, forms a complex with folded class I MHC molecules in the ER which is not retained but is transported to the cell surface. *EMBO J.* 16, 685–694.
- Lakomek, N.A., Ying, J., and Bax, A. (2012). Measurement of ¹⁵N relaxation rates in perdeuterated proteins by TROSY-based methods. *J. Biomol. NMR* 53, 209–221.
- Lange, O.F., and Baker, D. (2012). Resolution-adapted recombination of structural features significantly improves sampling in restraint-guided structure calculation. *Proteins* 80, 884–895.
- Lange, O.F., Rossi, P., Sgourakis, N.G., Song, Y., Lee, H.W., Aramini, J.M., Ertekin, A., Xiao, R., Acton, T.B., Montelione, G.T., and Baker, D. (2012). Determination of solution structures of proteins up to 40 kDa using CS-Rosetta with sparse NMR data from deuterated samples. *Proc. Natl. Acad. Sci. U S A* 109, 10873–10878.
- Leaver-Fay, A., Tyka, M., Lewis, S.M., Lange, O.F., Thompson, J., Jacak, R., Kaufman, K., Renfrew, P.D., Smith, C.A., Sheffler, W., et al. (2011). ROSETTA3: an object-oriented software suite for the simulation and design of macromolecules. *Methods Enzymol.* 487, 545–574.
- Lemmermann, N.A., Fink, A., Podlech, J., Ebert, S., Wilhelmi, V., Böhm, V., Holtappels, R., and Reddehase, M.J. (2012). Murine cytomegalovirus immune evasion proteins operative in the MHC class I pathway of antigen processing and presentation: state of knowledge, revisions, and questions. *Med. Microbiol. Immunol. (Berl.)* 201, 497–512.

- Li, H., Natarajan, K., Malchiodi, E.L., Margulies, D.H., and Mariuzza, R.A. (1998). Three-dimensional structure of H-2Dd complexed with an immunodominant peptide from human immunodeficiency virus envelope glycoprotein 120. *J. Mol. Biol.* **283**, 179–191.
- Lilley, B.N., and Ploegh, H.L. (2005). Viral modulation of antigen presentation: manipulation of cellular targets in the ER and beyond. *Immunol. Rev.* **207**, 126–144.
- Lu, X., Kavanagh, D.G., and Hill, A.B. (2006). Cellular and molecular requirements for association of the murine cytomegalovirus protein m4/gp34 with major histocompatibility complex class I molecules. *J. Virol.* **80**, 6048–6055.
- Mans, J., Natarajan, K., Balbo, A., Schuck, P., Eikel, D., Hess, S., Robinson, H., Simic, H., Jonjic, S., Tiemessen, C.T., and Margulies, D.H. (2007). Cellular expression and crystal structure of the murine cytomegalovirus major histocompatibility complex class I-like glycoprotein, m153. *J. Biol. Chem.* **282**, 35247–35258.
- Massi, F., Johnson, E., Wang, C., Rance, M., and Palmer, A.G., 3rd. (2004). NMR R1 rho rotating-frame relaxation with weak radio frequency fields. *J. Am. Chem. Soc.* **126**, 2247–2256.
- Natarajan, K., Hicks, A., Mans, J., Robinson, H., Guan, R., Mariuzza, R.A., and Margulies, D.H. (2006). Crystal structure of the murine cytomegalovirus MHC-I homolog m144. *J. Mol. Biol.* **358**, 157–171.
- Nilges, M. (1993). A calculation strategy for the structure determination of symmetric dimers by ¹H NMR. *Proteins* **17**, 297–309.
- Pervushin, K., Riek, R., Wider, G., and Wüthrich, K. (1997). Attenuated T2 relaxation by mutual cancellation of dipole-dipole coupling and chemical shift anisotropy indicates an avenue to NMR structures of very large biological macromolecules in solution. *Proc. Natl. Acad. Sci. U S A* **94**, 12366–12371.
- Pinto, A.K., Munks, M.W., Koszinowski, U.H., and Hill, A.B. (2006). Coordinated function of murine cytomegalovirus genes completely inhibits CTL lysis. *J. Immunol.* **177**, 3225–3234.
- Raman, S., Vernon, R., Thompson, J., Tyka, M., Sadreyev, R., Pei, J., Kim, D., Kellogg, E., DiMaio, F., Lange, O., et al. (2009). Structure prediction for CASP6 with all-atom refinement using Rosetta. *Proteins* **77** (Suppl 9), 89–99.
- Raman, S., Lange, O.F., Rossi, P., Tyka, M., Wang, X., Aramini, J., Liu, G., Ramelot, T.A., Eletsky, A., Szyperski, T., et al. (2010). NMR structure determination for larger proteins using backbone-only data. *Science* **327**, 1014–1018.
- Rao, T., Lubin, J.W., Armstrong, G.S., Tucey, T.M., Lundblad, V., and Wuttke, D.S. (2014). Structure of Est3 reveals a bimodal surface with differential roles in telomere replication. *Proc. Natl. Acad. Sci. U S A* **111**, 214–218.
- Reusch, U., Muranyi, W., Lucin, P., Burgert, H.G., Hengel, H., and Koszinowski, U.H. (1999). A cytomegalovirus glycoprotein re-routes MHC class I complexes to lysosomes for degradation. *EMBO J.* **18**, 1081–1091.
- Sass, H.J., Musco, G., Stahl, S.J., Wingfield, P.T., and Grzesiek, S. (2000). Solution NMR of proteins within polyacrylamide gels: diffusional properties and residual alignment by mechanical stress or embedding of oriented purple membranes. *J. Biomol. NMR* **18**, 303–309.
- Sgourakis, N.G., Lange, O.F., DiMaio, F., André, I., Fitzkee, N.C., Rossi, P., Montelione, G.T., Bax, A., and Baker, D. (2011). Determination of the structures of symmetric protein oligomers from NMR chemical shifts and residual dipolar couplings. *J. Am. Chem. Soc.* **133**, 6288–6298.
- Shen, Y., and Bax, A. (2012). Identification of helix capping and b-turn motifs from NMR chemical shifts. *J. Biomol. NMR* **52**, 211–232.
- Shen, Y., and Bax, A. (2013). Protein backbone and sidechain torsion angles predicted from NMR chemical shifts using artificial neural networks. *J. Biomol. NMR* **56**, 227–241.
- Shen, Y., Lange, O., Delaglio, F., Rossi, P., Aramini, J.M., Liu, G., Eletsky, A., Wu, Y., Singarapu, K.K., Lemak, A., et al. (2008). Consistent blind protein structure generation from NMR chemical shift data. *Proc. Natl. Acad. Sci. U S A* **105**, 4685–4690.
- Smith, L.M., McWhorter, A.R., Shellam, G.R., and Redwood, A.J. (2013). The genome of murine cytomegalovirus is shaped by purifying selection and extensive recombination. *Virology* **435**, 258–268.
- Svitel, J., Balbo, A., Mariuzza, R.A., Gonzales, N.R., and Schuck, P. (2003). Combined affinity and rate constant distributions of ligand populations from experimental surface binding kinetics and equilibria. *Biophys. J.* **84**, 4062–4077.
- Tolman, J.R., and Ruan, K. (2006). NMR residual dipolar couplings as probes of biomolecular dynamics. *Chem. Rev.* **106**, 1720–1736.
- Tomas, M.I., Kucic, N., Mahmutefendić, H., Blagojević, G., and Lucin, P. (2010). Murine cytomegalovirus perturbs endosomal trafficking of major histocompatibility complex class I molecules in the early phase of infection. *J. Virol.* **84**, 11101–11112.
- Tugarinov, V., and Kay, L.E. (2003). Ile, Leu, and Val methyl assignments of the 723-residue malate synthase G using a new labeling strategy and novel NMR methods. *J. Am. Chem. Soc.* **125**, 13868–13878.
- Tugarinov, V., Kanelis, V., and Kay, L.E. (2006). Isotope labeling strategies for the study of high-molecular-weight proteins by solution NMR spectroscopy. *Nat. Protoc.* **1**, 749–754.
- Tugarinov, V., Venditti, V., and Marius Clore, G. (2014). A NMR experiment for simultaneous correlations of valine and leucine/isoleucine methyls with carbonyl chemical shifts in proteins. *J. Biomol. NMR* **58**, 1–8.
- Varani, L., Bankovich, A.J., Liu, C.W., Colf, L.A., Jones, L.L., Kranz, D.M., Puglisi, J.D., and Garcia, K.C. (2007). Solution mapping of T cell receptor docking footprints on peptide-MHC. *Proc. Natl. Acad. Sci. U S A* **104**, 13080–13085.
- Vernon, R., Shen, Y., Baker, D., and Lange, O.F. (2013). Improved chemical shift based fragment selection for CS-Rosetta using Rosetta3 fragment picker. *J. Biomol. NMR* **57**, 117–127.
- Vink, C., Beuken, E., and Bruggeman, C.A. (2000). Complete DNA sequence of the rat cytomegalovirus genome. *J. Virol.* **74**, 7656–7665.
- Wang, J., Whitman, M.C., Natarajan, K., Tormo, J., Mariuzza, R.A., and Margulies, D.H. (2002). Binding of the natural killer cell inhibitory receptor Ly49A to its major histocompatibility complex class I ligand. Crucial contacts include both H-2Dd AND beta 2-microglobulin. *J. Biol. Chem.* **277**, 1433–1442.
- Wang, R., Natarajan, K., and Margulies, D.H. (2009). Structural basis of the CD8 alpha beta/MHC class I interaction: focused recognition orients CD8 beta to a T cell proximal position. *J. Immunol.* **183**, 2554–2564.
- Wang, R., Natarajan, K., Revilla, M.J., Boyd, L.F., Zhi, L., Zhao, H., Robinson, H., and Margulies, D.H. (2012). Structural basis of mouse cytomegalovirus m152/gp40 interaction with RAE1γ reveals a paradigm for MHC/MHC interaction in immune evasion. *Proc. Natl. Acad. Sci. U S A* **109**, E3578–E3587.
- Ward, A.B., Sali, A., and Wilson, I.A. (2013). Biochemistry. Integrative structural biology. *Science* **339**, 913–915.
- Warner, L.R., Varga, K., Lange, O.F., Baker, S.L., Baker, D., Sousa, M.C., and Pardi, A. (2011). Structure of the BamC two-domain protein obtained by Rosetta with a limited NMR data set. *J. Mol. Biol.* **411**, 83–95.
- Williams, A.F., and Barclay, A.N. (1988). The immunoglobulin superfamily—domains for cell surface recognition. *Annu. Rev. Immunol.* **6**, 381–405.
- Wüthrich, K. (1986). *NMR of Proteins and Nucleic Acids*. (New York: John Wiley).
- Zweckstetter, M., and Bax, A. (2001). Characterization of molecular alignment in aqueous suspensions of Pf1 bacteriophage. *J. Biomol. NMR* **20**, 365–377.

Note Added in Proof

Concurrently with the release of this work, the following article reported the 3.0 Å-resolution X-ray structure of the ectodomain of a very similar m04 strain sequence, including all functional glycosylations (PDB ID 4PN6). The structure is remarkably similar to our solution NMR model (backbone/heavy atom RMSD 0.6/0.8 Å, excluding the flexible loop at residues 95–102). Notably, the placement of the C-terminal helix (Figure 4) and loop conformation at residues 115–125 (Figure 5) are virtually identical in the X-ray structure. Given the unusual β-topology of the structure and lack of structural homologs in the PDB, this result highlights the power of the combined Rosetta/NMR approach in delivering highly accurate models at atomic resolution from a limited set of experimental restraints relative to conventional NMR methods.

Berry, R., Vivian, J.P., Deuss, F.A., Balaji, G.R., Saunders, P.M., Iin, J., Littler, D.R., Brooks, A.G., and Rossjohn, J. (2014). The structure of the cytomegalovirus-encoded m04 glycoprotein, a prototypical member of the mo2 family of immunoevasins. *J Biol Chem*. Published online June 30, 2014. <http://dx.doi.org/10.1074/jbc.M114.584128>.